

## TUTORIAL / ARTICLE DIDACTIQUE

**Design and construction of an efficient electro-optic modulator for laser spectroscopy****C. Mok, M. Weel, E. Rotberg, and A. Kumarakrishnan**

**Abstract:** We discuss design considerations and construction of a home-built electro-optic phase modulator (EOM) that can be used for locking a laser to an atomic transition. The EOM is designed to operate at a resonant frequency of  $\approx 20$  MHz and imposes a phase modulation on a laser beam. The phase-modulated light is sent through a reference cell containing a dilute gas of rubidium atoms. When the laser is scanned over an atomic resonance, the absorption of light through the cell can be detected and mixed down to DC to produce a dispersion shaped “error” signal. The error signal can be used to lock the laser to the atomic resonance. We also describe tests of the basic properties of the resonant circuit. The  $Q$  of the circuit is measured to be 10, resulting in 60% efficiency for the first-order sidebands at RF drive powers of 0.7 W. Applications include the spectroscopy of laser-cooled atoms.

PACS Nos.: 01.50.Pa, 39.25.+k 32.80.Pj, 42.62.Fi

**Résumé :** Nous discutons la conception et la construction dans notre laboratoire d’un modulateur de phase électro-optique (EOM) qui peut être utilisé pour synchroniser un laser sur une transition atomique. L’EOM est conçu pour opérer à une fréquence de résonance de  $\approx 20$  MHz et imposer une modulation de phase à un faisceau laser. Ce faisceau est envoyé dans une cellule contenant un gaz dilué d’atomes de rubidium. Quand le laser est analysé sur une résonance atomique, l’absorption de la lumière à travers la cellule peut être détectée et mélangée jusqu’à DC pour produire un signal d’erreur de forme dispersée. Ce signal d’erreur peut être utilisé pour synchroniser le laser sur la résonance atomique. Nous décrivons les tests effectués sur les caractéristiques de base du circuit résonant. Nous mesurons un  $Q$  de 10, ce qui donne une efficacité de 60 % pour les sidebands de premier ordre à une puissance RF de 0.7 W. Les applications incluent la spectroscopie d’atomes refroidis par laser.

[Traduit par la Rédaction]

Received 1 November 2005. Accepted 28 July 2006. Published on the NRC Research Press Web site at <http://cjp.nrc.ca/> on 26 September 2006.

**C. Mok, M. Weel, E. Rotberg, and A. Kumarakrishnan.**<sup>1</sup> Department of Physics, York University, 4700 Keele St., Toronto ON M3J 1P3, Canada.

<sup>1</sup>Corresponding author (e-mail: [akumar@yorku.ca](mailto:akumar@yorku.ca)).

## 1. Introduction

Tunable lasers have multiple wavelength-selecting elements such as piezo-controlled etalons and gratings. Typically, the length of the lasing cavity is controlled by a voltage sent to a piezo-electric transducer. The laser-cavity length can change because of a number of factors such as temperature changes, and mechanical vibrations. These factors affect the laser-frequency stability. The basic challenge in precision spectroscopy is to maintain a stable laser frequency [1].

The standard method of frequency-locking involves a two-step process outlined in ref. 2. An external Fabry–Perot cavity is used in a feedback loop to obtain a narrow line width of  $\sim 1$  MHz. The slow drift of the laser frequency is compensated by locking the laser to a reference point on an atomic spectral feature using a lock-in amplifier. A modulation frequency of the order of a few kHz is supplied to the scanning element of the laser. When the laser is scanned across the atomic resonance at a frequency that is much lower than the modulation frequency, the lock-in amplifier detects an absorption signal at the frequency of modulation and generates a dispersion-shaped DC error signal with a zero-crossing at the reference frequency. The error signal is continuously fed back to the laser, thereby correcting the laser frequency. We have recently reviewed the properties of lock-in amplifiers and outlined the construction of an inexpensive model in refs. 3 and 4.

A vapour cell containing a dilute gas of atoms is often used to obtain spectral lines that serve as a frequency reference. Since the spectral features are Doppler-broadened, the laser frequency can be stabilized only to a precision of a few tens of megahertz and is unsuitable for many applications in laser spectroscopy such as atom trapping. The widely used technique of saturated absorption [5] is used to obtain Doppler-free spectral features with a characteristic width of the order of the natural line width of the atomic transition  $\sim 10$  MHz.

Although lock-in amplifiers are widely used, an alternative technique involves the use of electro-optic phase modulators (EOMs) [6] to produce the dispersion-shaped error signal. The EOM can be used in the saturated absorption portion of the setup, thereby avoiding the need to modulate the laser frequency used in the experiment. The EOM produces a phase modulation of the laser beam that results in frequency sidebands. The interaction of the sidebands with the dilute gas produces the error signal. Typically, an EOM can be operated at radio frequencies of the order of the inverse of the atomic response time ( $\approx 100$  MHz). This is an obvious advantage for reducing  $1/f$  noise. We note that the modulation of the laser frequency used in the experiment can also be avoided using an acousto-optic modulator in the saturation absorption setup.

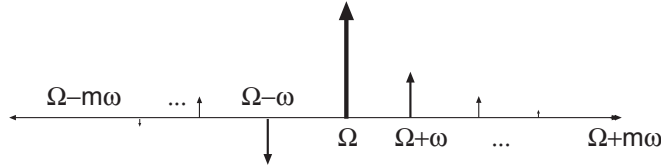
In this paper, we discuss the design and construction of an inexpensive EOM operating at a frequency of  $\sim 20$  MHz. The EOM consists of a resonant inductor, resistor, capacitor (LRC) circuit in which there is a wire-wound inductor and a distributed capacitor (EOM crystal). The energy is coupled into the circuit using a transformer arrangement. The rest of the paper is organized as follows. Section 2 contains a review of theoretical concepts. In Sect. 3, we explain the constraints of the design and the construction of the EOM. In Sect. 4, we present measurements of the quality factor of the resonant circuit and describe simple tests that validate the design. These include measurements of the sideband intensity and the dispersion shape used for locking the laser to the atomic resonance. In particular, we show that the efficiency of the sidebands is appreciable ( $\sim 60\%$  for a drive power of  $\sim 0.7$  W). This makes the device suitable for laser spectroscopy, and the design can also be adapted for use in upper-level undergraduate laboratory experiments.

## 2. Mathematical model

When a time-varying electric field is applied to the nonlinear crystal inside the EOM, the index of refraction  $n$  changes in a sinusoidal manner resulting in phase modulation of the laser beam passing through the crystal.

For the case where the incoming laser field is polarized along the  $x$  and  $y$  directions and propagates

**Fig. 1.** Frequency sidebands in the laser beam after passing through the electro-optic phase modulator.



along the  $z$  direction, a time varying electric field applied perpendicular to the direction of propagation results in a difference in the indices of refraction along the  $x$  and  $y$  directions. This results in a phase difference between these electric-field components that can be quantified by a parameter known as the index of modulation,  $M$ .

This phase shift produces frequency sidebands, with amplitudes that can be represented by [6, 7]

$$E(t) = E_0 \sum_{m=-\infty}^{\infty} J_m(M) \exp [it(\Omega + m\omega)] \tag{1}$$

Here,  $E_0$  is the amplitude of the incident laser-beam electric field,  $m$  is the order of the sidebands,  $\Omega$  is the incident laser frequency, and  $\omega$  is the drive frequency of the EOM. It is evident that the sidebands are shifted from the central frequency by integer multiples of the EOM drive frequency. The amplitude of each sideband is governed by a Bessel function of order  $m$ , as shown in Fig. 1. The argument of the Bessel function contains the index of modulation  $M$  given by [8]

$$M = \frac{\pi l n^3 r_x}{2d\lambda} V_{\text{cap}}(t) \tag{2}$$

where  $n$  is the unperturbed index of refraction of the crystal,  $r_x$  is the electro-optic coefficient for the specific orientation of the crystal,  $l$  is the length of the crystal,  $\lambda$  is the wavelength of light,  $d$  is the distance between the electrodes on the crystal, and  $V_{\text{cap}}$  is the voltage across the crystal. A detailed discussion of the electro-optic effect can be found in ref. 7.

For typical values of the crystal dimensions, the index of refraction and the electro-optic coefficient, the first-order frequency side bands have appreciable amplitudes even for relatively small values of  $M$  ( $M \ll 1$ ). In this case, only the central carrier frequency and the two first-order sidebands need to be considered. Taking the real components of the electric fields in (1),

$$\frac{E(t)}{E_0} = J_{-1}(M) \cos[(\Omega - \omega)t] + J_0(M) \cos(\Omega t) + J_1(M) \cos[(\Omega + \omega)t] \tag{3}$$

Noting that  $J_0(M) \approx \cos(M/2)$  and  $J_1(M) \approx \sin(M/2)$ , and applying the small-angle approximation, it can be shown that the electric field after the EOM is given by

$$\frac{E(t)}{E_0} = \cos(\Omega t) - \frac{M}{2} [\cos[(\Omega - \omega)t] - \cos[(\Omega + \omega)t]] \tag{4}$$

Alternatively, the incident electric field can be represented as  $E(t) = E_0 \cos[\Omega t + \phi(t)]$  where  $\phi(t)$  is the phase modulation due to the EOM, which can be written as  $\phi = M \sin(\omega t)$ . Here,  $M$  is the same modulation index as defined by (2) and represents the amplitude of phase modulation. Using the trigonometric identity for  $\cos(A + B)$ , we obtain

$$\frac{E(t)}{E_0} = \cos(\Omega t) \cdot \cos[M \sin(\omega t)] - \sin(\Omega t) \cdot \sin[M \sin(\omega t)] \tag{5}$$

Since  $M$  is much smaller than unity, we can apply the small-angle approximation  $\cos [M \sin(\omega t)] \approx 1$  and  $\sin [M \sin(\omega t)] \approx M \sin(\omega t)$ , so that

$$\frac{E(t)}{E_0} = \cos(\Omega t) + M \sin(\Omega t) \sin(\omega t) \quad (6)$$

Using the identity that  $\sin(A) \sin(B) = \frac{1}{2} [\cos(A + B) - \cos(A - B)]$ , the equation for the electric field after the EOM becomes

$$\frac{E(t)}{E_0} = \cos(\Omega t) - \frac{M}{2} [\cos[(\Omega - \omega)t] - \cos[(\Omega + \omega)t]] \quad (7)$$

which is identical to (4). Thus, it is possible to understand the physical meaning of (1). Figure 1 shows the relative amplitudes of the sidebands in (1). We note that the upper and lower sidebands in each order are out of phase by  $180^\circ$ .

When the laser beam from the EOM passes through a dilute atomic gas, the light is phase-shifted and attenuated. The transmitted electric field can be conveniently described by using exponential notation as in ref. 9.

$$\frac{E(t)}{E_0} = -\frac{MT_{-1}}{2} \exp[i(\Omega - \omega)t] + T_0 \exp[i\Omega t] + \frac{MT_{+1}}{2} \exp[i(\Omega + \omega)t] \quad (8)$$

Here,  $T_{-1,0,+1}$  are transmission coefficients for each of the frequency sidebands.

The  $m$ th transmission coefficient is defined as follows:

$$T_m = \exp[-\delta_m - i\phi_m] \quad (9)$$

where  $m$  denotes the sideband index,  $\delta_m$  is related to the frequency-dependent absorption coefficient of the gas  $\alpha_m$ , and  $\phi_m$  is the frequency-dependent phase shift due to the index of refraction of the gas near an atomic spectral line. The absorption coefficient is defined as

$$\delta_m = \alpha_m \cdot l \quad (10)$$

where  $l$  is the length of the sample. It is often convenient to represent  $\delta(\Omega)$  as a Lorentzian absorption profile represented by  $\delta(\Omega) \propto (1 + \Omega^2)^{-1}$ . The phase shift is related to the index of refraction  $n(\Omega)$  and can be expressed as

$$\phi_m \propto \frac{d\delta}{d\Omega} \quad (11)$$

Figure 2 shows the first-order sidebands when the laser beam is scanned across an atomic resonance.

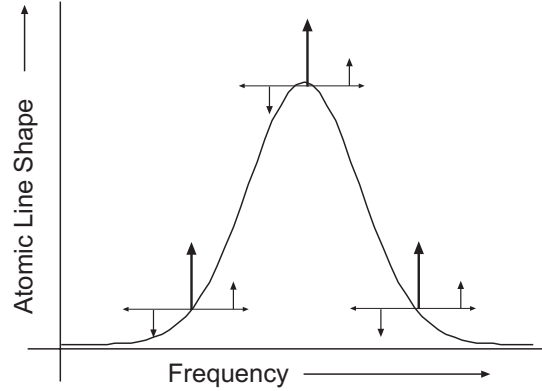
Using the definitions in (9), (10), and (11) in (8), we obtain

$$\begin{aligned} \frac{E(t)}{E_0} = \frac{M}{2} \exp[-\delta_{-1} - i\phi_{-1}] \cdot \exp[i(\Omega - \omega)t] + \exp[-\delta_0 - i\phi_0] \cdot \exp[i\Omega t] \\ - \frac{M}{2} \exp[-\delta_{+1} - i\phi_{+1}] \cdot \exp[i(\Omega + \omega)t] \end{aligned} \quad (12)$$

Taking the squared modulus of (12), and dropping terms of order  $M^2$ , we obtain an expression for the intensity of the beam transmitted by the sample

$$\begin{aligned} \frac{I(t)}{I_0} = 1 + [\exp[\delta_0 - \delta_{+1}] \cos(\phi_{+1} - \phi_0) - \exp[\delta_0 - \delta_{-1}] \cos(\phi_0 - \phi_{-1})] M \cos(\omega t) \\ + [\exp[\delta_0 - \delta_{+1}] \sin(\phi_{+1} - \phi_0) - \exp[\delta_0 - \delta_{-1}] \sin(\phi_0 - \phi_{-1})] M \sin(\omega t) \end{aligned} \quad (13)$$

**Fig. 2.** Position of sidebands at various points during the scan. The sideband closer to the peak of the spectral feature is absorbed more than the other sideband.



If the sidebands are close to the central frequency, the absorption and phase-shift functions are nearly the same for all frequency components. Hence,  $|\delta_0 - \delta_{+1}|$ ,  $|\delta_0 - \delta_{-1}|$ ,  $|\phi_0 - \phi_{+1}|$ , and  $|\phi_0 - \phi_{-1}|$  are much smaller than unity. We can then use the series expansion of  $e^x$  to first order, and use the small-angle approximation to obtain

$$\frac{I(t)}{I_0} = 1 + (\delta_{-1} - \delta_{+1})M \cos(\omega t) + (\phi_{+1} + \phi_{-1} - 2\phi_0)M \sin(\omega t) \quad (14)$$

This signal  $I(t)$ , is detected by a photodetector, multiplied with the RF signal used to drive the EOM (a process known as mixing) and low-pass-filtered to obtain the DC component of the signal. This is the dispersion-shaped error signal used for laser-frequency locking.

We consider three points on the scan in Fig. 2 for specific relative amplitudes for the sidebands. The photodiode outputs are shown in the left column of Fig. 3. When these signals are mixed with the in-phase and quadrature drive frequency, the results are shown in the central and right columns of Fig. 3.

We can understand the plots in Fig. 3 by noting that when the upper sideband ( $\Omega + \omega$ ) is attenuated by a dilute atomic gas, only the central frequency and lower sideband interact, creating a beat note. When the lower sideband ( $\Omega - \omega$ ) is attenuated, the central frequency and the upper sideband interact, and the intensity modulation is  $\pi$  phase-shifted. It is clear from Fig. 3 that when the laser is scanned across the atomic resonance, there will be a positive DC offset on one side of resonance, a negative offset on the other side, with a zero crossing at resonance. Both the in-phase and quadrature components of the mixed signal display this behaviour. This is indeed the shape of the feedback signal required to stabilize the laser frequency. As the laser is scanned across the atomic resonance, it is clear that there is a change in the DC value of the mixed signal. This effect occurs only in the presence of a dilute atomic gas. In the absence of the gas, the upper and lower sidebands in each order are out of phase by  $180^\circ$  and there will be no change in the DC value of the mixed signal.

When the signal from the photodetector given by (14) is mixed using the drive frequency of the EOM, we obtain

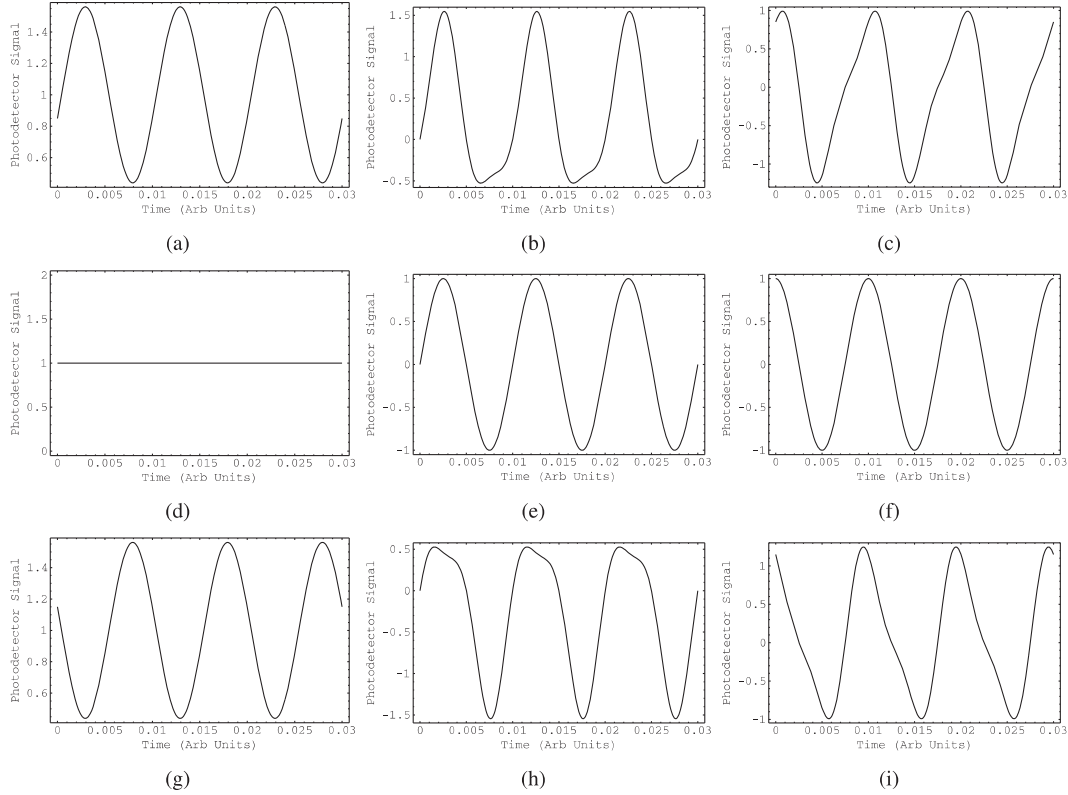
$$M_p(\Omega, t) = [1 + (\delta_{-1} - \delta_{+1})M \cos(\omega t) + (\phi_{+1} + \phi_{-1} - 2\phi_0)M \sin(\omega t)] \times \sin(\omega t) \quad (15)$$

for the in phase component and

$$M_q(\Omega, t) = [1 + (\delta_{-1} - \delta_{+1})M \cos(\omega t) + (\phi_{+1} + \phi_{-1} - 2\phi_0)M \sin(\omega t)] \times \cos(\omega t) \quad (16)$$

for the quadrature component.

**Fig. 3.** Left column: Photodiode signal. Center column: In-phase portion of mixed signal. Right column: Quadrature portion of mixed signal. Top row: below-resonance peak, Center row: at atomic resonance, Bottom row: above resonance peak. These figures were generated using (15) and (16). The modulation index is assumed to be 0.75.



If the mixed signals in (15) and (16) are sent through a low-pass filter, we obtain the following expressions for the in-phase and quadrature components of the error signal:

$$S_p(\Omega) = \int_{t=t_0}^{t=t_0+2\pi/\omega} \sin(\omega t) [1 + (\delta_{-1} - \delta_{+1})M \cos(\omega t) + (\phi_{+1} - \phi_{-1} - 2\phi_0)M \sin(\omega t)] dt \quad (17)$$

$$S_p(\Omega) = \frac{M}{2} (\phi_{+1} - \phi_{-1} - 2\phi_0) \quad (18)$$

$$S_q(\Omega) = \int_{t=t_0}^{t=t_0+2\pi/\omega} \cos(\omega t) [1 + (\delta_{-1} - \delta_{+1})M \cos(\omega t) + (\phi_{+1} - \phi_{-1} - 2\phi_0)M \sin(\omega t)] dt \quad (19)$$

$$S_q(\Omega) = \frac{M}{2} (\delta_{-1} - \delta_{+1}) \quad (20)$$

The low-pass filter averages the signal temporally, essentially integrating the signal over one cycle. Carrying out the integration filters out the DC terms expressed in (17) and (19). These are the error signals that can be used to correct the laser frequency. The dispersion shapes given by the theoretical model are shown in Fig. 4 and the in-phase and quadrature components have distinct shapes. Figure 4 was generated using (10), (11), (18), and (20). The quadrature component is related the differential absorption of the sidebands, and the in-phase component is related to the differences of the indices of refraction for the sidebands.

**Fig. 4.** Theoretical dispersion shapes assuming a Lorentzian absorption profile,  $\delta(\omega) = 1/(1 + \omega^2)$ , and index of refraction  $\phi(\omega) = d\delta/d\omega$ . (a) Dispersion shape generated by differential absorption,  $S_q$ . (b) Dispersion shape generated by differential phases,  $S_p$ . The shapes are distinct when the EOM drive frequency is increased.

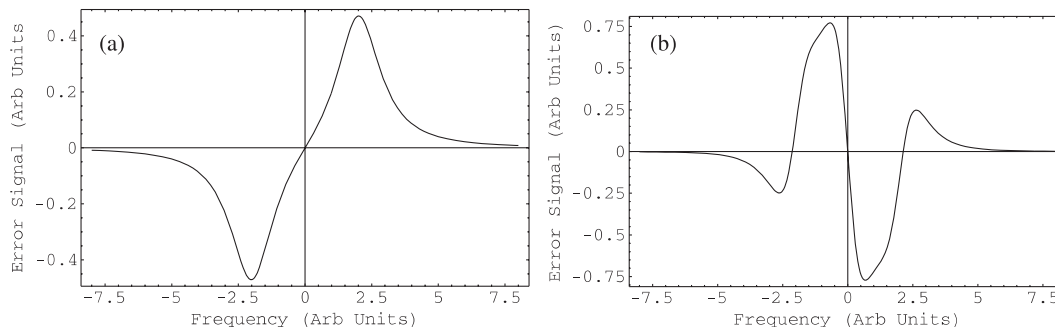
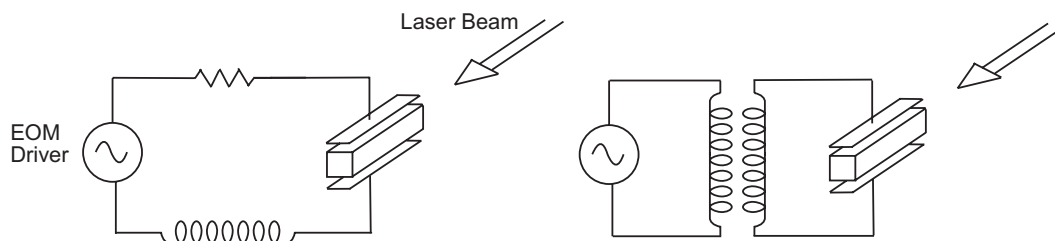


**Fig. 5.** Simplified diagram of EOM resonant circuit. Left: Simple series LRC circuit. Right: Transformer method. The primary coil is connected to the EOM driver, and the secondary coil is connected across the EOM crystal.



### 3. Construction

Here we will discuss the design considerations and constraints associated with the construction of the EOM. The Doppler-free atomic resonances from the saturated absorption discussed in the introduction are power-broadened and have a typical linewidth of  $\sim 10$  MHz. To see the sidebands clearly, the resonant frequency of the EOM should be somewhat larger than 20 MHz. If the resonant frequency is much larger, the dispersion shapes will no longer behave linearly near the lock point. Our goal is to use a low-power RF source of  $< 1$  W to drive the EOM. This can be accomplished with a LRC circuit with a resonant frequency  $\omega_0 = 1/\sqrt{LC}$  so that the RF output is amplified within the circuit. The EOM cavity consists of an electro-optic crystal that serves as a distributed capacitor, and a wire wound inductor such that the circuit has a  $50\Omega$  impedance, matching the output impedance of the RF source. Thus, the resulting electric field is suitably large across the electro-optic crystal. Figure 5 shows two possibilities for assembling the circuit.

The electro-optic crystal is 10 mm long, and has a 1 mm square cross section. The end faces of the crystal are antireflection coated for the wavelength  $\lambda = 780$  nm and the top and bottom faces have gold-plated electrodes. Based on (2), the phase shift  $\phi(t) = M \sin(\omega t)$  applied across the crystal faces can be written as

$$\phi(t) = \beta \xi l \tag{21}$$

where  $\beta = \pi n^3 r_{33} / \lambda$  and  $\xi$  is the RF electric field. The numerical value of  $\beta$  is defined by the choice of

electro-optic crystal and the operating wavelength. We use lithium tantalate as the electro-optic crystal for which  $n = 2.18$  and  $r_{33} = 35.8$  pm/V, so that  $\beta \sim 1.3 \times 10^{-3}/V$ .

Using  $V = E \cdot d$ , where  $V$  is the voltage across the crystal length, and  $d$  is the thickness of the crystal, we can estimate the value of  $V$  when  $\phi = \pi$ . For the resonant circuit shown on the left of Fig. 5, the voltage across the crystal  $V_{\text{cap}} = I(j\omega L) + IR$  where  $I$  is the current in the circuit and  $R$  is the effective resistance. The  $Q$  factor of this resonant circuit can be approximated as  $\omega L/R$ , for  $Q \gg 1$  so that  $V \sim I\omega L$ . Thus,  $V^2 = 2PQ/\omega C$  where  $P$  is the average power delivered by the RF source.

Since the crystal can be approximated as a parallel plate capacitor with capacitance  $C = \epsilon\epsilon_0 WI/d$ , we obtain

$$V^2 = \frac{2PQ}{\omega_0\epsilon\epsilon_0} \frac{d}{WI} \quad (22)$$

Here,  $\epsilon = 43$  is the dielectric constant and  $W$  is the width of the crystal (1 mm). Using (21) and (22), with  $\omega_0 = 2\pi(20 \times 10^6)$  and  $Q = 10$ , we obtain  $P \sim 0.2$  W. The challenge associated with the construction is to obtain a  $Q \sim 10$  and simultaneously meet the impedance-matching requirement.

We estimated the crystal capacitance to be 3.8 pF, and this value was confirmed using a commercial capacitance meter ( $4.2$  pF  $\pm 5\%$ ). Since the resonant frequency and capacitance are constraints, we require an inductor of  $\sim 20$   $\mu\text{H}$  to obtain a resonance frequency of  $\sim 20$  MHz. The inductor was wound using 168 turns of magnet wire of 0.5 mm diameter, and connected in series with the crystal capacitor. A drive-frequency range of 1 – 100 MHz was generated by mixing the RF outputs of two commercial 150 MHz voltage-controlled oscillators, and filtering out the sum frequency. A 1 W broad-band RF amplifier with a 50  $\Omega$  output impedance was used to amplify the oscillator output and drive the EOM. Since the impedance of such a series circuit nears zero at the resonant frequency, a 50  $\Omega$  resistor is necessary to ensure the amplifier is appropriately terminated. However, this would reduce the cavity  $Q$  by a factor of 2, and require a 40% increase in RF amplifier power. To solve this problem, we assembled a transformer with a 400 nH primary coil coupled with the 20  $\mu\text{H}$  inductor connected to the crystal, as shown in Fig. 5. The impedance of the 400 nH inductor was  $\sim 50$   $\Omega$  at the resonant frequency. The exact values of these inductors were fine-tuned by trial and error. These components were placed in a copper box to improve RF shielding and reduce losses. The input impedance of the EOM was measured to be 56.5  $\Omega$  at the resonant frequency. It should be noted that in designing EOMs to operate at higher frequencies, additional precautions are necessary to prevent RF losses. Reference 10 describes the challenges associated with the construction of an EOM operating at  $\sim 1$  GHz.

#### 4. Experimental set-up and results

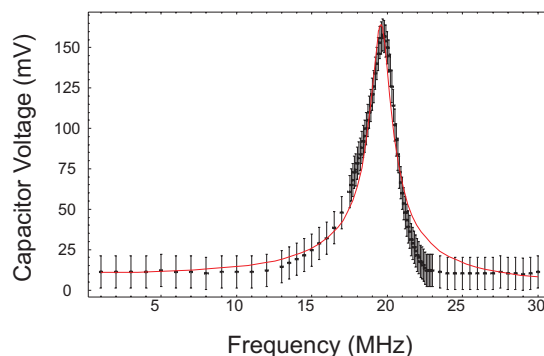
To validate the design, the  $Q$  factor was determined by measuring the voltage across the capacitor as a function of the drive frequency. For these measurements, a 4 dBm amplifier was used so that the RF oscillator was isolated the EOM. Figure 6 shows the peak-to-peak voltage  $V_{\text{cap}}$  across the capacitor as a function of RF frequency  $f$ . The effective impedance of the circuit is  $Z = \sqrt{R^2 + (L2\pi f - \frac{1}{C2\pi f})^2}$  so that the total current through the circuit is  $I = V/Z$  as given by Ohm's law. The voltage across the capacitor  $V_{\text{cap}}$  is then  $I X_c$  where  $X_c$  is the impedance of the capacitor. Thus,  $V_{\text{cap}}$  can be represented as

$$V_{\text{cap}}(f) = \frac{A}{Z} \quad (23)$$

where  $A$  is a constant.

The continuous line in Fig. 6 shows a fit to the data based on the model in (23). The free parameters associated with the fit are the circuit resistance  $R$ ,  $L$ , and  $C$ . Here,  $A$  is proportional to the maximum voltage at the resonant frequency. The fit parameters  $R = 65 \pm 1\Omega$ ,  $C = 2.8 \pm 0.1$  pF, and  $L = 22.8 \pm 0.1$   $\mu\text{H}$  are in reasonable agreement with independent measurements. These parameters give a

**Fig. 6.** Resonance circuit response. The peak occurs at  $\approx 19.8$  MHz, and the  $Q$  factor is 10. Best fit parameters are  $R = 65 \pm 1\Omega$ ,  $C = 2.8 \pm 0.1$  pF, and  $L = 22.8 \pm 0.1$   $\mu$ H.



resonant frequency of 19.8 MHz, which is consistent with the separation of the sidebands observed in separate experiments discussed in this section. The  $Q$  of the circuit can be estimated using  $Q = f/\Delta f$ , where  $\Delta f$  is the full width half maximum of the frequency response curve. In this case, we obtain  $Q = 10$ . The estimates in Sect. 3 suggest that it should be possible to obtain appreciable sideband intensity with RF drive power  $< 1$  W. An alternate technique to measure the sideband intensity is given in ref. 11.

The experimental setup to measure the EOM efficiency and use the EOM for laser stabilization is shown in Fig. 7. Approximately 2 mW of laser power was diverted from the laser to a saturated absorption spectrometer. The setup consists of a glass plate that serves as a beam splitter to create a weak probe beam, a rubidium reference cell and a 50–50 beam splitter and a photodiode. The pump and probe beams, as labelled in Fig. 7, counter-propagate inside the rubidium cell. The EOM is placed in the probe-beam path as shown. The probe beam is incident on a high-speed photodiode ( $\sim 1$  ns rise time) and the signal is mixed with the RF oscillator used to drive the EOM. A variable cable length serves as a phase shifter. The mixed down signal is low-pass filtered, and fed back to the laser to complete the feedback loop.

In the presence of the rubidium cell, the laser frequency can be scanned across an atomic resonance, so that the amplitudes of the sidebands can be measured directly as a function of RF power. The saturated absorption spectrum consists of peaks riding on top of a Doppler background. In Fig. 8, the laser is scanned across the  $F = 3 \rightarrow F' = 4$  atomic transition in  $^{85}\text{Rb}$ . With the EOM off, we observe the Doppler-free resonance. The typical widths of the spectral peaks are  $\sim 10$  MHz, which represents the power-broadened linewidth. With an RF drive power of 0.7 W applied to the EOM, we observe the presence of sidebands in the absorption spectrum. As the laser is scanned, the frequency sidebands interact sequentially with the vapour. The frequency axis is calibrated on the basis of the known hyperfine splittings in the Rb spectrum. As discussed in Sect. 2 and 3, it can be seen that the maximum sideband intensity occurs in the estimated range  $\Omega_0 \pm \omega$  where  $\omega = 19.8$  MHz is the resonant frequency of the EOM.

It is clear from Fig. 8 that the total efficiency of the two first-order sidebands is appreciable ( $\sim 60\%$ ) even for modest drive powers of  $\sim 0.7$  W. Based on fits to (23), the relative heights of the peaks suggest that the modulation index  $M = 1.36$  for a RF drive power of 0.681 W. Using the electro-optic parameters for lithium tantalate,  $\text{LiTaO}_3$ , we can estimate the  $Q$  of the cavity to be  $\sim 11$  using (1), (2), and (21).

It is possible to detect the presence of sidebands even for relatively low RF drive powers ( $\ll 1$  W) by Fourier analysis of the signal from the photodetector. However, it is particularly instructive to see the presence of sidebands directly as in Fig. 8 using a drive power of  $\sim 0.5$  W. The efficiency of the EOM can be demonstrated by plotting the integrated signal associated with the sidebands as a function

**Fig. 7.** Experimental setup. Continuous lines with single arrows show paths of laser light. Broken lines with double arrows indicate paths of electronic signals. The Opamp circuit has a gain of  $\sim 3000$ .

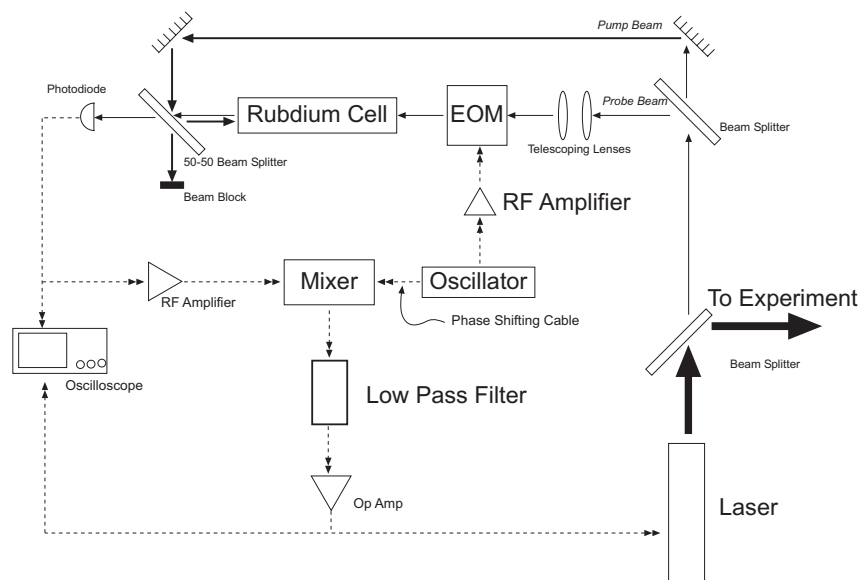
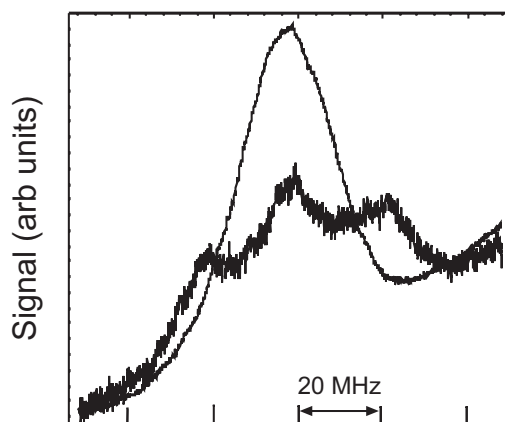


**Fig. 8.** Oscilloscope traces of the photodiode output when the laser is scanned over the  $F = 3 \rightarrow F' = 4$  transition in  $^{85}\text{Rb}$ . The width of this curve is determined by power-broadening as explained in ref. 3. We have used the known splitting between Rb spectral lines to convert the time axis into frequency units. The smooth curve is obtained with the EOM off and involved an average of 128 sweeps. With the EOM on, the amplitude of the original peak is reduced, and secondary peaks appear. The RF power applied is 0.7 W. The signal was averaged over only eight sweeps to prevent laser drifts from obscuring the sidebands.



of the RF drive power. This is shown in Fig. 9. The broken line represents the predictions for the intensity  $J_m^2(\sqrt{P})$  where  $P$  is the RF drive power. These predictions assume the absence of higher order sidebands. We observe that the data are better represented by a function  $\propto J_m^2(P)$ . We attribute this effect to the value of the modulation index becoming comparable to unity for the range of RF powers used in these measurements. When  $M$  is large compared to unity, the distribution of energy into the higher order sidebands cannot be ignored and this effect depletes the carrier intensity more rapidly

**Fig. 9.** Intensity of laser frequency as a percentage of incident intensity, measured from the Doppler-free resonances. Left: Carrier intensity, continuous line is  $J_0^2(P)$ , broken line is  $J_0^2(\sqrt{P})$  Right: First-order sideband intensity. Continuous line is  $J_{\pm 1}^2(P)$ , broken line is  $J_{\pm 1}^2(\sqrt{P})$  where  $P$  is the RF drive power.

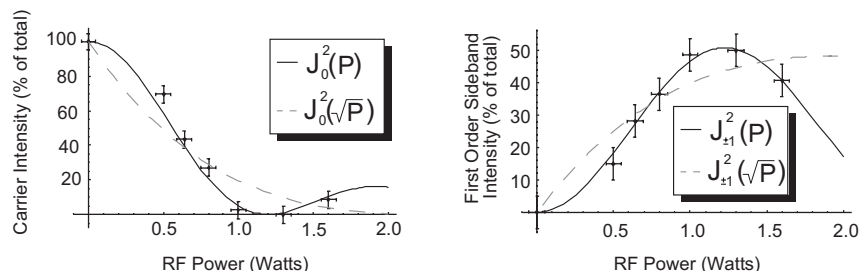
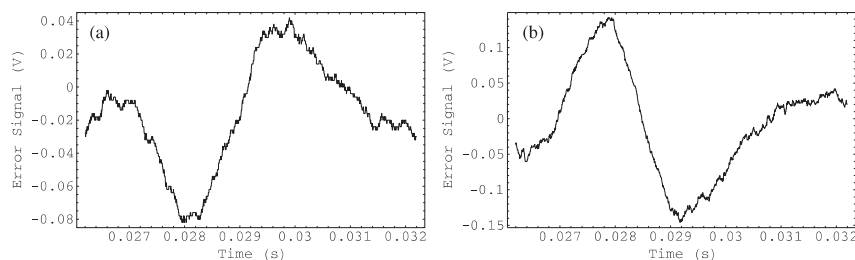


**Fig. 10.** Error signal produced by the feedback loop when the laser is scanned over the  $F = 3 \rightarrow F' = 3-4$  cross-over peak. The phase was varied by  $90^\circ$  using the phase-shifting cable shown in Fig. 7. The graph on the right has a steeper slope in the vicinity of the zero crossing.



than for the case when  $M$  is small. Similarly, the intensity of the first-order sideband increases more rapidly than suggested by the theoretical treatment that ignores higher order terms. We have confirmed these trends using a commercial EOM operating at 3 GHz. The experiment involved measuring the amplitude of the sidebands that were widely separated and much better resolved than in Fig. 8. Thus, it was possible to detect sidebands with sufficient signal-to-noise for small values for  $M$ . The results show that the sideband intensity scales as  $J^2(\sqrt{P})$  for  $M \ll 1$ , and that it scales as  $J^2(P)$  as  $M$  becomes comparable to unity.

Figure 10 shows the dispersion-shaped error signal produced when the laser is scanned over the  $F = 3 \rightarrow F' = 3-4$  cross-over peak in  $^{85}\text{Rb}$ . The rubidium spectrum and the origin of the cross-over peaks are explained in refs. 3 and 6. The dispersion shapes resemble the theoretical predictions in Fig. 4. The phase of the signal can be varied by altering the length of the phase-shifting cable shown in Fig. 7. As explained in refs. 3 and 4, the feedback signal can be used to stabilize the laser frequency for atom-trapping applications. For each of the error signals shown in Fig. 10, a particular RF phase will bring the laser toward the atomic resonance and a  $180^\circ$  phase shift will invert the shape of the error signal and push the laser away from resonance. If the EOM drive frequency is increased, the distinction between the shapes becomes more apparent. In general, the error signal produced by the differential phases is preferred for laser-locking since it has a steep slope at the atomic resonance.

## 5. Conclusions

We have designed an efficient electro-optic modulator that operates at  $\sim 20$  MHz with a  $Q$  factor of  $\sim 10$ . The device produces appreciable sideband intensity for modest RF drive powers of the order of 0.5 W. The cost of the device is  $\sim \$700$  and this is essentially determined by the price of the antireflection-

**Table 1.** List of components and prices.

	Component	Unit cost (\$)
	Leysop $1 \times 1 \times 10$ mm LiTaO <sub>3</sub> Crystal	700
EOM	Copper inductor wire	—
	Copper box	—
	2 × minicircuits ZOS-50 VCO	140
	minicircuits ZP-10514 mixer	70
Driver	minicircuits BLP-100 filter	35
	minicircuits ZFL-500 amplifier	80
	minicircuits ZHL-1A amplifier	250
	1" Glass plate	
	2 × 1" mirror	
Setup	50–50 Beam splitter	
	2 Collimating lenses	
	Rubidium vapor cell	
	Thorlabs DET 210 high-speed photodiode	

coated crystal. A breakdown of the cost of components is found in Table 1. The low cost would permit extensive use in undergraduate laboratory experiments.

### Acknowledgements

We would like to acknowledge the contributions of Kristian Kostecky in the initial phase of this work. This work was supported by Canada Foundation for Innovation, Ontario Innovation Trust, the Natural Sciences and Engineering Research Council of Canada, Photonics Research Ontario, and York University.

### References

1. W. Demtroder. *Laser spectroscopy: basic concepts and instrumentation*. Springer Verlag, Berlin. 1981.
2. W.P. Drever, J.L. Hall, F.V. Kowalski, J. Hough, G.M. Ford, A.J. Munley, and H. Ward. *Appl. Phys. B*, **31**, 97 (1983).
3. M. Weel and A. Kumarakrishnan. *Can. J. Phys.* **80**, 1449 (2002).
4. K. Sowka, M. Weel, S. Cauchi, L. Cockins, and A. Kumarakrishnan. *Can. J. Phys.* **83**, 907 (2005).
5. T.W. Hänsch, I.S. Shahin, and A.L. Schawlow. *Phys. Rev. Lett.* **27**, 707 (1971).
6. M.D. Levenson and S. Kano. *Introduction to nonlinear laser spectroscopy*. Boston Academic Press, Boston. 1988.
7. C. Davis. *Lasers and electro-optics: fundamentals and engineering*. Cambridge University Press, Cambridge. 1996.
8. A. Yariv. *Quantum electronics*. John Wiley and Sons, New York. 1967.
9. G. Bjorklund. *Opt. Lett.* **5**, 15 (1980).
10. J.F. Kelly and A. Gallagher. *Rev. Sci. Instrum.* **58**, 563 (1987).
11. T. Milkaelian, M. Weel, A. Kumarakrishnan, P.R. Battle, and R.C. Swanson. *Can. J. Phys.* **81**, 639 (2003).